nanomaterials

MDPI

Article

Enhanced Solar Light Photocatalytic Activity of Ag Doped TiO_2–Ag_3PO_4 Composites

Abdessalem Hamrouni [1], Hanen Azzouzi [1], Ali Rayes [1], Leonardo Palmisano [2], Riccardo Ceccato [3] and Francesco Parrino [3,*]

[1] Laboratoire de Recherche Catalyse et Matériaux pour l'Environnement et les Procédés URCMEP (UR11ES85), Faculté des Sciences de Gabès, Université de Gabès, Campus Universitaire Cité Erriadh, Gabès 6072, Tunisia; hamrouni-28@hotmail.fr (A.H.); hanenazzouzi408@gmail.com (H.A.); ali.rayes@fsb.rnu.tn (A.R.)

[2] Department of Engineering, University of Palermo, Viale delle Scienze, Ed. 6, 90128 Palermo, Italy; leonardo.palmisano@unipa.it

[3] Department of Industrial Engineering, University of Trento, Via Sommarive 9, 38123 Trento, Italy; riccardo.ceccato@unitn.it

* Correspondence: francesco.parrino@unitn.it

Received: 24 March 2020; Accepted: 14 April 2020; Published: 21 April 2020

Abstract: Composites comprised of Ag_3PO_4 and bare TiO_2 (TiO_2@Ag_3PO_4) or silver doped TiO_2 (Ag@TiO_2–Ag_3PO_4) have been synthesized by coupling sol–gel and precipitation methods. For the sake of comparison, also the bare components have been similarly prepared. All the samples have been characterized by X-ray diffraction (XRD), UV-vis diffuse reflectance spectroscopy (DRS), scanning electron microscopy (SEM), Fourier transformed infrared spectroscopy (FTIR), photoelectrochemical measurements, and specific surface area (SSA) analysis. The optoelectronic and structural features of the samples have been related to their photocatalytic activity for the degradation of 4–nitrophenol under solar and UV light irradiation. Coupling Ag_3PO_4 with silver doped TiO_2 mitigates photocorrosion of the Ag_3PO_4 counterpart, and remarkably improves the photocatalytic activity under solar light irradiation with respect to the components, to the TiO_2–Ag_3PO_4 sample, and to the benchmark TiO_2 Evonik P25. These features open the route to future applications of this material in the field of environmental remediation.

Keywords: Ag@TiO_2–Ag_3PO_4 heterojunction; solar photocatalysis; 4–nitrophenol degradation; sol–gel synthesis

1. Introduction

Each year, the surface of Earth receives 3850000 EJ of solar energy. However, only 0.014% of it is currently exploited to cover the energy demand, and to face environmental issues [1]. In fact, efficient solar light conversion is one of the hot topics of our society, which is finally aware of the need to develop and actuate sustainable processes to mitigate the dramatic climate changes and environmental disaster we are the witness of in the last years. The unique properties of visible light active semiconductors allow one to use them to convert solar energy into photogenerated charges, which, in turn, enable electricity generation or trigger useful chemical reactions. In this way, it is possible to mimic nature by storing solar energy in chemical bonds, by producing high value-added chemical compounds in a "green" way, or by removing hazardous compounds through their photoinduced mineralization. Titanium dioxide (TiO_2) has been widely investigated and used to this aim, mainly due to its remarkable photoactivity, low cost, and robustness. However, TiO_2 can be only activated upon UV light irradiation, which represents only ca. 5% of the solar light spectral emission. In order to overcome this limitation, TiO_2 has been variously modified to extend its light absorption range toward the visible light region [2].

In many cases sensitization of TiO_2 under visible light is achieved by modifying its surface with dyes [3], chromogenic species [4], or metal nanoparticles [5]. However, the resulting materials are often poorly stable, with few exceptions [6], and mainly useful for niche applications rather than for environmental remediation, where large effluent volumes need to be treated. Bulk modification, instead, provides more stable materials [7]. However, the influence of bulk defectivity on the recombination rate of the photogenerated charges, and in turn on the photocatalytic activity, is still object of scientific debate [8] due to the highly specific nature of the photoactive materials and of their interaction with light [9]. Alternatively, intrinsically visible light active semiconductors such as oxides [10], chalcogenides [11], and mixed semiconductors [12–16] have been recently investigated to trigger photocatalytic reactions under visible light irradiation [17]. Among them, the p-type semiconductor silver orthophosphate (Ag_3PO_4) has been often reported as a promising alternative to visible light active TiO_2-based materials in the field of solar photocatalysis. The narrow band gap energy enables its visible light activation, and the strong oxidizing power [18–20] justifies its extensive investigation in scientific reports dealing with organic dye degradation, bacterial disinfection, and water splitting reaction [18,19,21]. In particular, quantum efficiency up to 90% can be achieved for O_2 evolution under visible light irradiation in the presence of Ag_3PO_4. Worth of mention is also the great versatility of Ag_3PO_4, whose morphology can be easily tuned by opportunely adjusting the synthesis procedure. For instance, Zwara et al. [22] recently reported the synthesis of variously shaped Ag_3PO_4 samples with high photoactivity for the degradation of phenol under visible light. However, Ag_3PO_4 is prone to photocorrosion because photogenerated electrons easily reduce lattice silver ions to metallic silver eventually destroying the photocatalyst after few working cycles [23]. The photostability of Ag_3PO_4 can be enhanced in various ways. Some authors proposed the use of sacrificial reducing agents to hinder photocorrosion. However, this reduces the energy stored in the bonds of the products, which is particularly detrimental for water splitting [24] or for synthetic applications [25]. A much suitable approach consists in coupling different semiconductors [12–16]. To this aim, p–n heterostructures of Ag_3PO_4 and TiO_2 are particularly promising. Yao et al. [26] reported the enhanced visible light photocatalytic activity of Ag_3PO_4 nanoparticles deposited onto commercial TiO_2 (Evonik P25). In this case, degradation of dyes such as methylene blue and rhodamine B have been used as model visible light reactions, so that it is difficult to assess if a direct or indirect photocatalytic process is taking place [27]. However, results were confirmed by Rawal et al. [28], which used a homemade polycrystalline TiO_2 coupled with Ag_3PO_4 for the visible light degradation of 2–propanol in gas phase. Teng et al. [29] reported the synthesis of ordered TiO_2 nanotubes decorated with Ag_3PO_4 and Ag nanoparticles, and tested the composites for the removal of 2–chlorophenol in aqueous solution. Silver nanoparticles, deposited on the surface of Ag_3PO_4, acted as electron sinks thus preventing photocorrosion [30,31]. However, in the latter case, the photocatalyst is a ternary composite ($Ag–Ag_3PO_4–TiO_2$) presenting exposed silver nanoparticles, which can aggregate and be easily removed during real waste water treatments. With the aim of simplifying the system for environmental applications, by providing higher robustness and simultaneously maintaining visible light absorption and high photoactivity, in the present investigation we introduced silver into the lattice of TiO_2 and designed a binary heterojunction between Ag_3PO_4 and nanostructured $Ag@TiO_2$. This composite provides efficient charge separation due to the unique optoelectronic features of the $Ag@TiO_2$ counterpart, and high photocatalytic activity under solar light irradiation. In particular, the photocatalytic degradation of 4–nitrophenol (4–NP) under UV and natural solar light irradiation have been investigated, and the activity results have been related to the physico-chemical features of the samples.

2. Materials and Methods

2.1. Synthesis of the Samples

Ag_3PO_4 was synthesized according to a simple precipitation protocol. Silver nitrate ($AgNO_3$, Park scientific, Northampton, UK 99.8%) and monosodium phosphate ($NaH_2PO_4{\cdot}2H_2O$, Merck, Darmstadt,

Germany, extra pure) salts were employed as sources of Ag^+ and PO_4^{3-} ions, respectively. Two aqueous solutions of Ag^+ (0.1 M) and PO_4^{3-} (0.3 M) were prepared separately, and 246 mL of the silver solution were added dropwise to 330 mL of the orthophosphate solution in order to provide large excess of the PO_4^{3-} anions. The obtained yellow precipitate was separated by centrifuge, washed several times with distilled water, and finally dried at 80 °C overnight.

TiO_2 was synthesized by dissolving 11.3 mL of titanium isopropoxide ($Ti[OCH(CH_3)_2]_4$, Sigma Aldrich, St. Louis, MO, USA, 97%) in 11.4 mL isopropanol (C_3H_7OH, 99.8%, Sigma Aldrich, St. Louis, MO, USA). Hydrolysis started by adding 2.15 mL of acetic acid (CH_3COOH, Sigma Aldrich, St. Louis, MO, USA, glacial 99.5%) and 1.35 mL distilled water, corresponding to molar ratio n_{H_2O}/n_{Ti} equal to 2. The resulting solution was stirred at 70 °C for about 20 min, until a white gel was obtained. The gel was then dried at 100 °C overnight and the resulting powder was calcined at 400 °C for 3 h in static air.

Silver doped TiO_2 ($Ag@TiO_2$) was synthesized following the same procedure used for bare TiO_2, but dissolving in the starting isopropanol solution an opportune amount of silver nitrate to reach an Ag/Ti molar ratio equal to 0.01. Notably, the percentage of silver used in this work is the optimum one in terms of photocatalytic activity and stability, as demonstrated in previous reports [32–37].

The composites TiO_2–Ag_3PO_4 and $Ag@TiO_2$–Ag_3PO_4 were synthesized by dispersing the as prepared TiO_2 and $Ag@TiO_2$, respectively, in the 0.1 M monosodium phosphate aqueous solution just before the addition of the 0.1 M $AgNO_3$ solution, and by following the same procedure described for the preparation of the Ag_3PO_4 sample. The molar percentage of TiO_2 (bare and silver doped) and Ag_3PO_4 was 25% and 75%, respectively, in both the composites. All the above mentioned chemicals were used as received without further purification.

2.2. Characterization

X-ray diffraction (XRD) analysis of the samples has been performed by using a Rigaku D-Max III powder diffractometer, Tokyo, Japan, in Bragg–Brentano geometry, working between 10 and 70° (2θ range) with sampling step of 0.05° and a counting time of 2 s. Monochromatic Cu Kα radiation was used, operating at a voltage of 40 kV and a current of 30 mA; a curved graphite monochromator was inserted in the diffracted beam. Both quantitative analysis and crystallite size determination were performed by means MAUD software® (Version 2.26, by Luca Lutterotti, University of Trento, 2010) [38,39], by combining the Rietveld-based method for the determination of weight percentages of phases, and line profile analysis based on the Warren–Averbach theory for the evaluation of mean crystallite sizes (D) and microstrains (ε).

UV-visible diffuse reflectance spectra were recorded by a Perkin Elmer Lambda 950 UV-vis spectrophotometer, Waltham, MS, USA, equipped with an integrating sphere, in the range of 190–800 nm and by using barium sulfate ($BaSO_4$, Sigma Aldrich, St. Louis, MO, USA, p.a.) as the reference. Reflectance (R_∞) was converted by the instrument software to $F(R_\infty)$ values according to the Kubelka–Munk theory. The bandgap was obtained from a plot of $[F(R_\infty)h\nu]^{1/2}$ vs. the energy of the exciting light, by assuming that all of the photocatalysts are indirect semiconductors. The band gap energy (E_g) values were determined by extrapolating the linear part of the plot to the x axis.

Scanning electron microscopy (SEM) and energy dispersive X-Ray spectroscopy (EDS) analyses were carried out using a field emission-scanning electron microscope (FE-SEM, Supra 40/40VP, Zeiss, Oberkochen, Germany), operating at a voltage of 20 kV on specimens upon which a thin layer of Pt/Pd had been deposited under Ar atmosphere. Fourier transformed infrared spectroscopy (FTIR) was carried out on a Thermo Nicolet Avatar 330 FTIR, Thermo Fisher, Waltham, MS, USA, spectrophotometer.

To determine the specific surface area (SSA) and the pore size distribution (PSD) of the photocatalysts, nitrogen adsorption measurements were performed at the liquid nitrogen temperature by using a Micromeritics, Norcross, GA, USA, ASAP 2010 porosimeter. All the samples were degassed below 1.3 Pa at 200 °C prior to the measurement. SSA's were calculated by the Brunauer−Emmet−Teller (BET) equation in the P/P^0 interval 0.05–0.33. PSD's were calculated by using the Barrett Joyner Halenda (BJH) method applied both on the adsorption and desorption branches of the isotherms.

Determination of the flat band potential of selected samples was performed in a Pyrex round bottom flask (V = 150 mL) irradiated with a 500 W medium pressure mercury lamp. 100 mg of the photocatalyst were dispersed into 100 mL of a 0.1 M KNO_3 solution. The working electrode was a platinum foil and an Ag/AgCl electrode was used as the reference. The suspension was irradiated under nitrogen bubbling for 30 min and then 20 mg of MV^{2+} (1,1′–dimethyl–4,4′–bipyridinium dichloride) or DP^{2+} (4,5–dihydro–3a,5a–diaza–pyrene dibromide) were added as the electron scavengers. A pH meter Thermo Orion (Thermo Scientific, Waltham, MS, USA 720A and a multimeter Metex 3800 (Metex Corp., Seoul, South Korea) were used to measure the values of pH and the potential (V), respectively. Potentiometric titration was carried out by adjusting the pH with HNO_3 and NaOH solutions.

2.3. Photocatalytic Experiments

A Pyrex tubular photoreactor (V = 100 mL) was used for the photodegradation tests of 4–nitrophenol (4–NP, Sigma Aldrich, St. Louis, MO, USA, 98%). In a representative run the reactor contained 80 mL of an aqueous solution of 4–NP at a concentration of 10 $mg \cdot L^{-1}$ in which 80 mg of the photocatalyst were dispersed. The catalyst amount of 1 $g \cdot L^{-1}$ enabled the safe comparison of the results obtained in the presence of different samples. A magnetic stirrer ensured the homogeneity of the reaction mixture. The suspension was kept in the dark under agitation during 60 min prior to irradiation, in order to reach the adsorption–desorption equilibrium. Samples were taken at different time intervals and filtered using a 0.2 μm Millipore filter to separate the photocatalyst. The concentration of 4–NP during irradiation time was measured by using a Perkin Elmer 950 UV-vis spectrophotometer, Waltham, MS, USA. Tests under UV light irradiation were performed by using six Philips (Amsterdam, The Netherlands) FSL BL T8 lamps (10 W each) axially positioned around the photoreactor, with the main emission peak at 365 nm. The radiation power absorbed per unit volume of the suspension was about 0.76 $mW \cdot mL^{-1}$ measured by a Delta Ohm photo quantum meter (model HD9021) (Selvazzano Dentro, Italy) with a LP 9021 UVA sensor probe. 4–NP photodegradation tests under solar light were carried out by exposing to natural sun light at the same time as many different reactors in the presence of the investigated samples, during a sunny day in Gabes (Tunisia, 33°53′24″N 10°06′36″E) between 11 am and 4 pm in June. This approach allows one to safely compare the photocatalytic activity of the samples under natural solar light, as all of the photoreactors worked under the same irradiation conditions. The photocatalytic results have been compared with those obtained in the presence of commercial TiO_2 P25 (Evonik). The mean sun light intensity during the solar photocatalytic runs was 8.2 $W \cdot m^{-2}$ in the range 315–400 nm, and 2800 $\mu E \cdot m^{-2} \cdot s^{-1}$ in the range 400–700 nm.

3. Results

3.1. Structure and Morphology of the Samples

Figure 1 reports the XRD patterns of Ag_3PO_4, Ag@TiO_2, and Ag@TiO_2–Ag_3PO_4 samples. The XRD patterns of TiO_2 and of TiO_2–Ag_3PO_4 are reported in the Supporting Information (Figures S1–S4), being similar to those of Ag@TiO_2 and Ag@TiO_2–Ag_3PO_4, respectively.

Ag_3PO_4 presents body centered cubic structure (JCPDS N°06-0505) while bare TiO_2 shows the typical patterns of the anatase structure (JCPDS N°21-1272). Ag_3PO_4 signals were sharper with respect to those of TiO_2 indicating the lower crystallinity of the latter, typical of powders obtained from the sol–gel method. The Ag@TiO_2 sample presents qualitatively the same patterns of the TiO_2 sample indicating that the anatase structure is not affected upon silver doping (Ag/Ti molar ratio = 0.01). Moreover, no traces of impurities ascribable to silver containing compounds such as oxides can be observed, suggesting the successful incorporation of silver into the TiO_2 lattice. On the basis of XRD data, the lattice parameters (a, b, and c) and the mean crystallites dimension (D) were calculated for the pure components as summarized in Table 1, which also reports the microstrain values (ε), the specific surface area (SSA), and the pores volume (V_p).

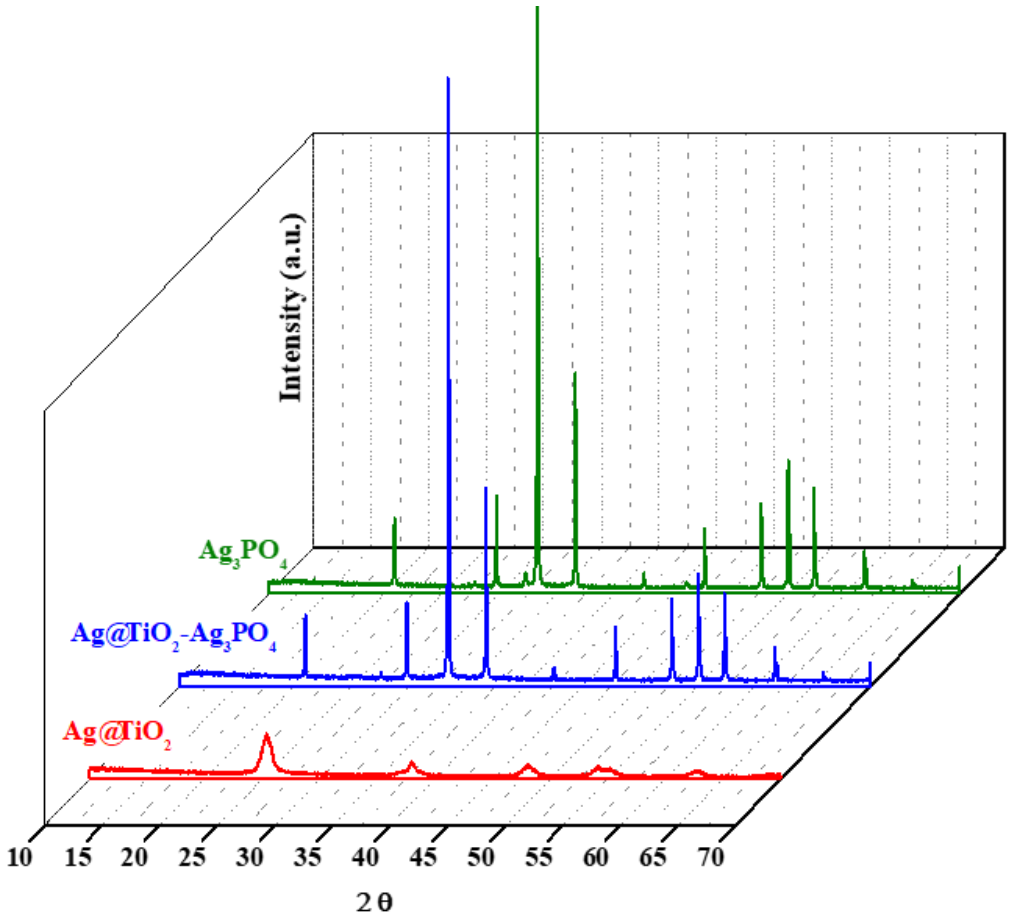

Figure 1. XRD patterns of Ag_3PO_4, $Ag@TiO_2$, and $Ag@TiO_2$–Ag_3PO_4 composites.

Table 1. Lattice parameters (a, b, and c), mean crystallites dimension (D), microstrain values (ε), specific surface area (SSA and BET), and pores volume (V_p) of the samples indicated. Digits under brackets represent relative error influencing the last significant digit of the calculated value.

Samples	a (Å)	b (Å)	c (Å)	D (nm)	ε	SSA ($m^2 \cdot g^{-1}$)	V_p ($cm^3 \cdot g^{-1}$)
Ag_3PO_4	6.0209(1)	6.0209(1)	6.0209(1)	332(8)	-	0.5	0.003
TiO_2	3.7911(3)	3.791	9.523(1)	26.1(4)	0.00288(3)	80	0.205
$Ag@TiO_2$	3.794(1)	3.794	9.499(3)	23.6(8)	0.0058(2)	54	0.109
TiO_2–Ag_3PO_4	-	-	-	-	-	1.9	0.005
$Ag@TiO_2$–Ag_3PO_4	-	-	-	-	-	1.7	0.004

By comparing the lattice parameters and the crystallite size of TiO_2 and $Ag@TiO_2$ in Table 1, it is evident that in the presence of silver the unit cell shrinked along c and became larger along a and b directions. These changes, due to an isotropic size dependent effect [40], can be attributed to the insertion of substitutional silver ions into the TiO_2 lattice. In fact, the bigger size of Ag^+ (1.26 Å) with respect to that of Ti^{4+} ions (0.60 Å) modifies the lattice parameter and influences the crystal growth and the particle size. Literature reports suggest that silver doping generally hinders the growth of crystallites [41] due to grain boundary restraining caused by symmetry-breaking effects of the dopant [36]. At the same time, a decrease in crystallite dimensions is associated to an increase of microstrain values, reported in Table 1, due to the presence of surface tensions that provoke an increase of stresses [42]. This is confirmed also in this work, being the size of particles slightly smaller in the

silver doped TiO_2 with respect to the bare sample. Similar effects have been observed in literature when doping metal oxides with other metal ions [43].

The specific surface area of Ag_3PO_4 sample is much lower than that of the TiO_2-based ones, in agreement with its higher crystallinity observed by XRD analysis. The mixed samples present intermediate specific surface area, closer to that of Ag_3PO_4, which is present in a higher amount with respect to TiO_2.

The morphology and the composition of the samples were investigated by using scanning electron microscopy (SEM). Figure 2 shows the SEM images of all the samples. EDS analyses, reported in the Supporting Information (Figure S5a–c), confirm the presence of the expected atoms in percentage relatively close to the estimated one. No impurities containing foreign atoms could be detected. Images of TiO_2 and $Ag@TiO_2$ samples do not present significant differences, and are composed of micrometric agglomerates comprised of small nanoparticles of few tens of nanometers. This is in agreement with the crystallites dimension retrieved by XRD analysis. On the other hand, the Ag_3PO_4 particles are in the range of 1 to 5 micrometers and appear quite homogeneous in morphology and size. The composites TiO_2–Ag_3PO_4 and $Ag@TiO_2$–Ag_3PO_4 are comprised, respectively, of large TiO_2 or $Ag@TiO_2$ agglomerates upon which Ag_3PO_4 particles can be observed.

Infrared spectra of the samples are shown in Figure 3.

The spectra of the Ag_3PO_4 containing samples present a signal at 1649 cm^{-1} and a broad band between 3000 and 3600 cm^{-1} that can be attributed to the bending and to the stretching of O–H groups of adsorbed water, respectively [44,45]. The characteristic peaks of the PO_4^{3-} groups are present at 1010 cm^{-1} and 558 cm^{-1} corresponding to P–O stretching vibrations [44,45]. The IR spectra of TiO_2 and $Ag@TiO_2$ present a broad band between 500 and 900 cm^{-1}, ascribable to Ti–O vibrations [46].

3.2. Optical Properties

The absorption spectra of the samples are presented in Figure 4a. The values of $F(R_\infty)$, calculated according to the Kubelka–Munk theory from the values of diffuse reflectance, were proportional to the absorbance. By considering that all of the samples are indirect crystalline semiconductors [47], the band gap energy can be obtained by extrapolating the linear part of a plot of $[F(R_\infty)h\nu]^{1/2}$ vs. the energy of the exciting light (Figure 4b).

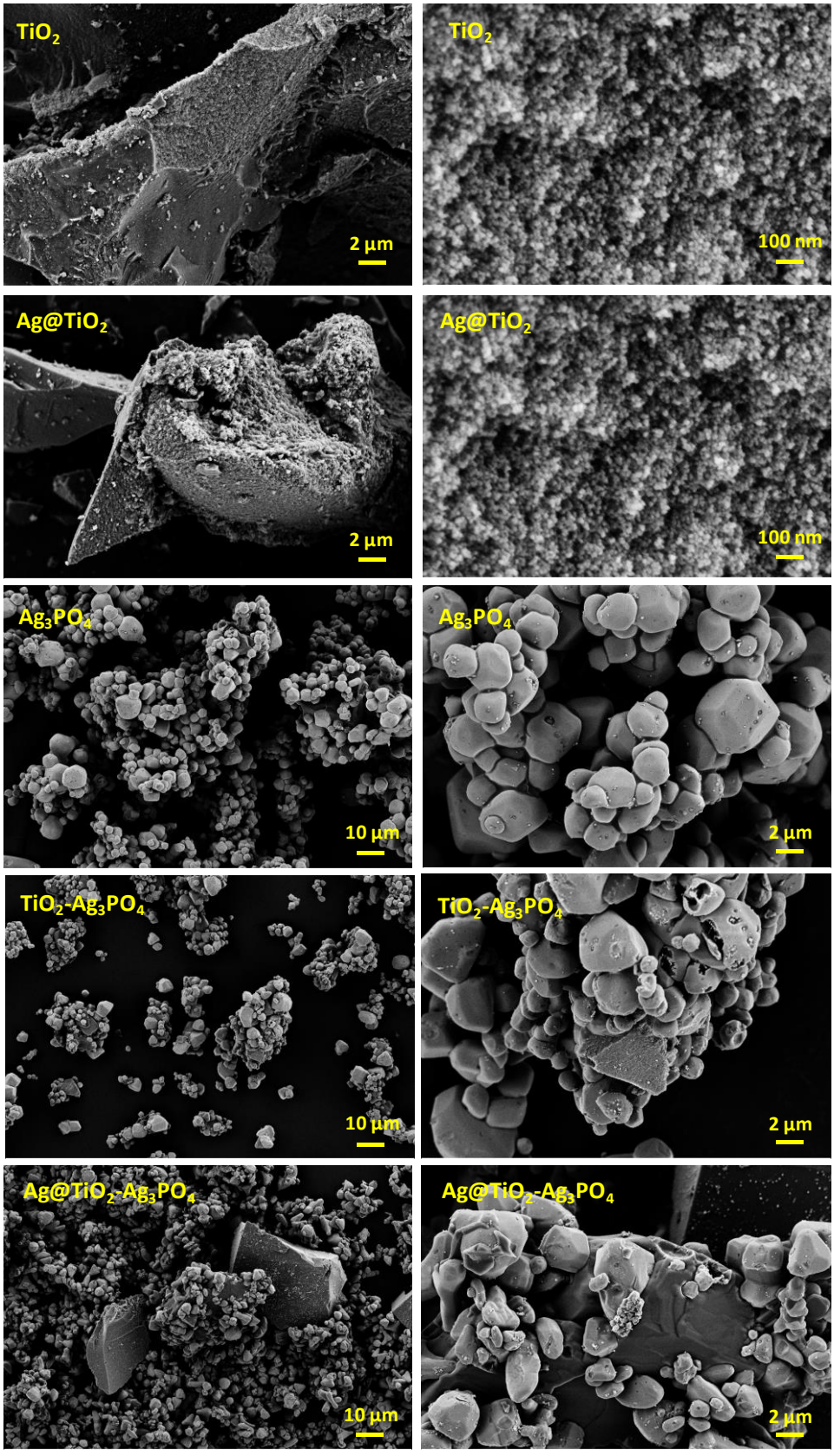

Figure 2. SEM images of TiO_2, $Ag@TiO_2$, Ag_3PO_4, TiO_2–Ag_3PO_4, and $Ag@TiO_2$–Ag_3PO_4 samples.

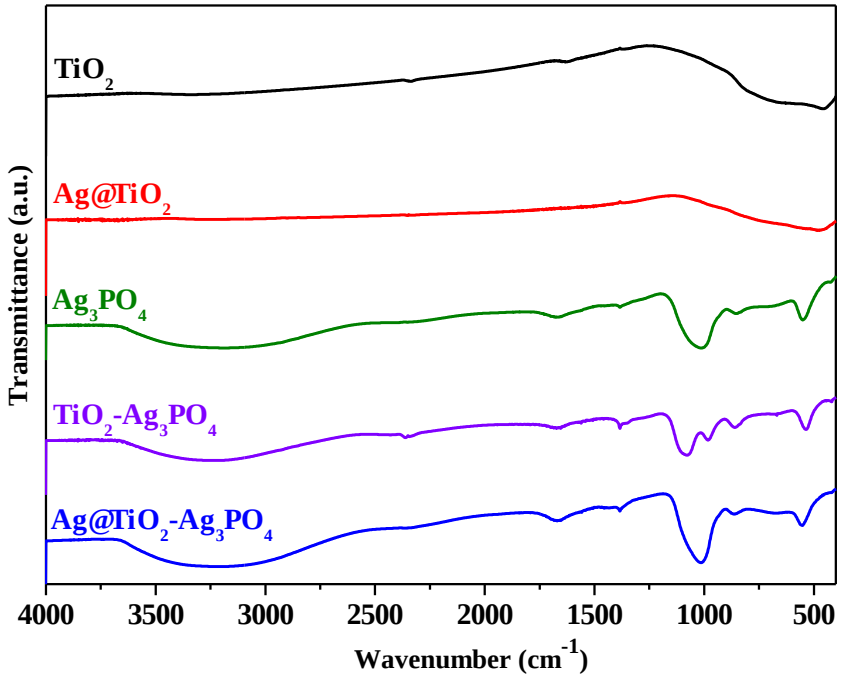

Figure 3. FTIR spectra of TiO_2 (black spectrum), $Ag@TiO_2$ (red spectrum), Ag_3PO_4 (green spectrum), TiO_2–Ag_3PO_4 (purple spectrum), and $Ag@TiO_2$–Ag_3PO_4 (blue spectrum) samples.

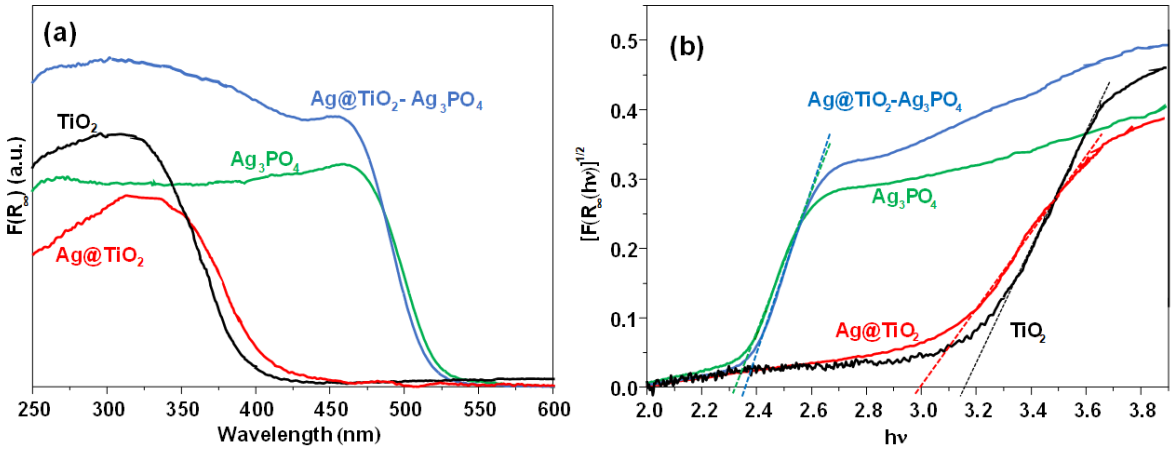

Figure 4. (**a**) UV-vis absorption spectra and (**b**) Tauc plot of the TiO_2 (black line), $Ag@TiO_2$ (red line), Ag_3PO_4 (green line), and $Ag@TiO_2$–Ag_3PO_4 (blue spectrum) samples.

The adsorption edge of the Ag_3PO_4 containing samples is at about 540 nm due to the narrow band gap of this semiconductor. The conduction band of Ag_3PO_4 presents Ag 5s and 5p character, while the valence band is composed of Ag 4d and O 2p orbitals [48,49]. As expected, $Ag@TiO_2$–Ag_3PO_4 sample presented lower absorption in the visible region with respect to bare Ag_3PO_4, but higher absorption in the UV region due to the typical transition of TiO_2. By comparing the spectra of bare TiO_2 and of $Ag@TiO_2$, it was evident the red shift of the doped sample moved towards the visible region due to the presence of silver ions into the lattice. Notably, the $Ag@TiO_2$ spectrum does not show the typical plasmon resonance of silver nanoparticles. This is a further evidence of the successful incorporation of silver ions into the lattice of TiO_2. The introduction of silver ions, in fact, is reported to introduce intermediate energy states deriving from the strong electronic coupling between the orbitals of TiO_2 and of silver. In particular, spin polarized density of states analysis revealed strong

hybridization between the silver orbitals and the Ti 3d and O 2p bands near the Fermi level [50]. The delocalized electron cloud results in a strong bonding between Ag atoms and the oxygen of TiO_2. This strongly interacting electronic structure results in a bathochromic shift of the absorption edge, similarly to what reported for strongly interacting components of a solid solution, as in the case of vanadium, chromium, iron, or nickel doped TiO_2 prepared by ion implantation [51] or for Fe_2O_3 heterojunctions with ZnO [16] and TiO_2 [52]. This behavior significantly differs from the more common weak interaction case, as in the case of silver islands on the surface of TiO_2, usually generating novel absorption shoulders. According to the Kubelka–Munk theory the band gap energy of bare Ag_3PO_4, TiO_2–Ag_3PO_4, and Ag@TiO_2–Ag_3PO_4 was ca. 2.3 eV, while the band gap of TiO_2 and Ag@TiO_2 were 3.2 and 3.0 eV, respectively. The narrow band gap of the Ag@TiO_2 with respect to TiO_2 makes it a better candidate to be part of a visible light active heterojunction with Ag_3PO_4. However, the knowledge of the potential edge of the photogenerated electrons is required to establish the nature of the interfacial electron transfer between the components. To this aim we experimentally determined the quasi Fermi level of both Ag@TiO_2 and TiO_2 samples by means of the method proposed by Roy et al. [53]. This method allows one to estimate the quasi Fermi level of a powdered semiconductor in water suspension and under irradiation, i.e., under experimental conditions similar to those used during the photocatalytic experiments. In fact, increasing the pH of the suspension under irradiation shifts cathodically the band edges of the semiconductor, until the one-electron reduction of the electron scavenger is thermodynamically allowed. This occurs at the inflection point of the potentiometric curve, where the quasi Fermi level of electrons equals the pH independent reduction potential of the electron acceptor.

Trials to determine the quasi Fermi level of Ag_3PO_4 with this method failed, so that we used the conduction band edge reported in literature (0.45 V vs. NHE at pH 7) [54,55]. Figure 5a,b show the photovoltage vs. pH curves obtained by irradiating TiO_2 and Ag@TiO_2 suspensions in the presence of MV^{2+} and DP^{2+}, respectively, as the electron acceptors. The use of DP^{2+} instead of MV^{2+} was necessary because in the presence of MV^{2+} the flex point would have been evident at too high pH values (ca. 9). Notably, the determination of the quasi-Fermi level of electrons of TiO_2 does not depend on the nature of the electron scavenger used, as demonstrated by Kisch et al. [56].

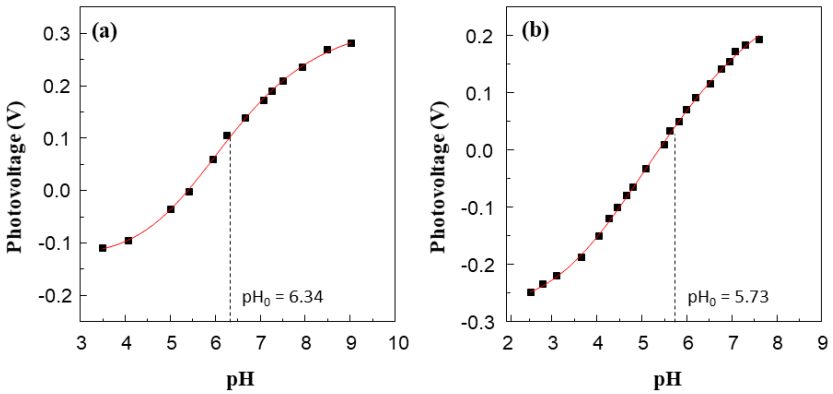

Figure 5. Effect of pH on the photovoltage developed by irradiation of aqueous suspension of TiO_2 (**a**) and Ag@TiO_2 (**b**) in the presence of MV^{2+} and DP^{2+}, respectively, as electron scavengers. Each experiment has been repeated 3 times and reproducibility was better than ± 0.02 V.

The pH values of the inflection point (pH_0) of the obtained sigmoidal titration curves, i.e., pH_0 equal to 6.34 and 5.73 for TiO_2 and Ag@TiO_2 samples, allow one to calculate the flat band potential at pH 7 using Equation (1):

$$E_{FB}\ (pH = 7) = E_{EA^{2+}/EA^{+\cdot}} + 0.059\ (pH_0 - 7) \quad (1)$$

where $E_{EA^{2+}/EA^{+\cdot}}$ is the standard potential of the electron acceptor used, i.e., $MV^{2+}/MV^{+\cdot}$ equal to −0.45 V vs. NHE and $DP^{2+}/DP^{+\cdot}$ equal to −0.27 V vs. NHE [54]. The resulting potentials of the photogenerated electrons were −0.5 and −0.34 V for TiO_2 and $Ag@TiO_2$, respectively.

By taking into account these values, the one reported in literature for Ag_3PO_4 [54,55], and the measured band gap energies, the simplified electronic map of the two heterojunctions $Ag@TiO_2$–Ag_3PO_4 and TiO_2–Ag_3PO_4, shown in Figure 6, can be proposed.

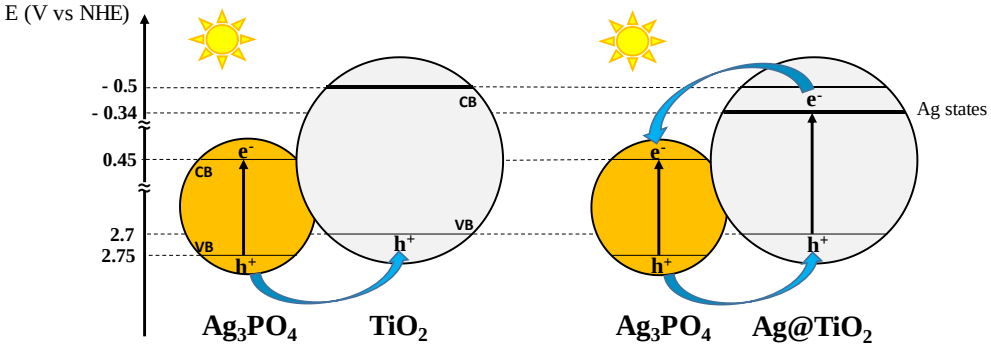

Figure 6. Mechanism of charge separation in the systems TiO_2–Ag_3PO_4 and $Ag@TiO_2$–Ag_3PO_4. Notably, under solar light irradiation also excitation of bare TiO_2 take place, even if at lower extent due to the low fraction of UV photons (ca. 5%) in the solar light. For this reason, and for the sake of clarity, Figure 6 does not show this effect.

The visible part of the solar spectrum is not able to excite the TiO_2 counterpart of the TiO_2–Ag_3PO_4 sample, while the presence of substitutional silver within the bulk of $Ag@TiO_2$ enables visible light excitation of the $Ag@TiO_2$ nanoparticles in the $Ag@TiO_2$–Ag_3PO_4 sample. In both the composites the photogenerated charges are efficiently separated; however, the excitation of the $Ag@TiO_2$ counterpart enables generation of electrons at the silver intermediate energy states from which they can be more efficiently injected into the conduction band of Ag_3PO_4.

3.3. Photocatalytic Activity under UV and Natural Solar Light Irradiations

Figure 7 shows the photodegradation of the 4–NP under UV light (Figure 7a) and under natural solar light (Figure 7b) in the presence of the investigated photocatalysts. For the sake of comparison, results obtained in the presence of the commercial TiO_2 P25 Evonik are also reported.

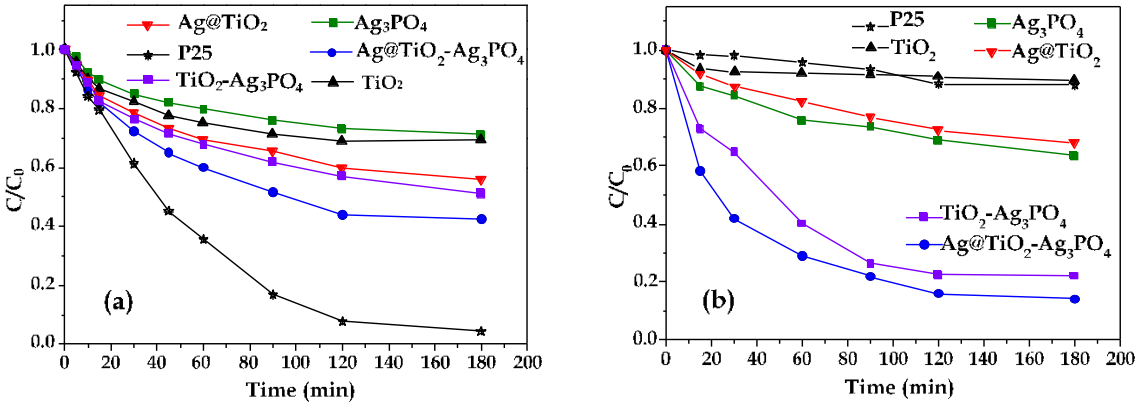

Figure 7. Normalized concentration of 4–NP during the irradiation time (**a**) under UV light and (**b**) under natural solar light of the (■) Ag_3PO_4, (▼) $Ag@TiO_2$, (▲) TiO_2, (*) P25, (●) $Ag@TiO_2$–Ag_3PO_4, and (■) TiO_2–Ag_3PO_4 samples.

The observed initial rate constants (k_{obs}) for each run in Figure 7 have been calculated by differentiating the experimental data at the initial time. The obtained values are reported in Table 2.

Table 2. Observed initial rate constants (k_{obs} ($mg \cdot L^{-1} \cdot min^{-1}$)) of 4–NP degradation under UV and natural solar light irradiation in the presence of the considered photocatalytic powders.

$k_{obs} \cdot 10^2$	Ag_3PO_4	TiO_2	P25	$Ag@TiO_2$	TiO_2–Ag_3PO_4	$Ag@TiO_2$–Ag_3PO_4
UV light	6.8	8.8	15.8	10.4	11.1	12.6
Solar light	6.8	3.8	0.6	5.5	13.5	26.9

Under UV light (Figure 7a), the commercial P25 was the most active sample. The composites, and in particular the $Ag@TiO_2$–Ag_3PO_4 one, were more active than TiO_2, Ag_3PO_4, and $Ag@TiO_2$ samples. Ag_3PO_4 showed the lowest activity despite its narrow band gap. The situation dramatically changes under solar light irradiation (Figure 7b), which mainly contains visible light photons, being the UV component only ca. 5%. TiO_2 and P25 samples were poorly active under solar light, according to their optical properties, while the presence of substitutional silver into the lattice of $Ag@TiO_2$ endows it with higher photocatalytic activity, comparable with that of Ag_3PO_4. Moreover, the composites, and in particular the $Ag@TiO_2$–Ag_3PO_4 one, were the most active samples. Notably, Ag doping almost doubles the initial degradation rate in the $Ag@TiO_2$–Ag_3PO_4 sample with respect to the TiO_2–Ag_3PO_4 one.

It is known that coupling Ag_3PO_4 with TiO_2 mitigates the photocorrosion of the Ag_3PO_4 counterpart [29]. In order to check if the same holds also for the $Ag@TiO_2$–Ag_3PO_4 under UV light, three photocatalytic runs were consecutively performed by using the same powder recovered after each cycle. Results are shown in Figure 8.

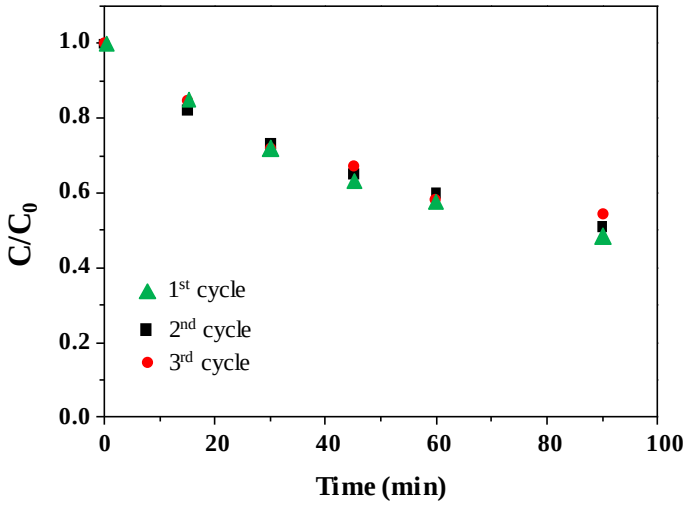

Figure 8. Normalized concentration of 4–NP during the irradiation time for three consecutive photocatalytic runs in the presence of the same $Ag@TiO_2$–Ag_3PO_4 powder recovered after each cycle.

The superior activity of the $Ag@TiO_2$–Ag_3PO_4 photocatalyst reflects the above discussed charge transfer mechanism (Figure 6). The existence of heterojunctions between TiO_2 and Ag_3PO_4 has been already reported to enhance photocatalytic activity of the composites with respect to the components. In fact, it is known that the close contact between two semiconductors of suitable electronic structure triggers interfacial electron transfer, effective spatial separation and longer life time of the photogenerated charges, which in turn account for the higher activity. This mechanism can be also invoked in the present case for both the $Ag@TiO_2$–Ag_3PO_4 and TiO_2–Ag_3PO_4 systems. In fact, the suitable relative position of the valence and conduction bands in both cases allows migration of the

holes generated under visible light irradiation in the valence band of Ag_3PO_4 to the valence band of TiO_2. However, in this paper we highlight that silver modification of the TiO_2 counterpart results in an even higher activity under solar light irradiation. In fact, according to the DRS results, silver doping enables the visible absorption of the $Ag@TiO_2$ material, so that under solar light irradiation it is possible to generate higher amount of excitons localized on both $Ag@TiO_2$ and Ag_3PO_4. Moreover, in this case electrons generated into the conduction band (or into intermediate energy states) of $Ag@TiO_2$ can also migrate toward the conduction band of Ag_3PO_4 thus enhancing the spatial charge separation. Finally, these effects not only account for the improved photocatalytic activity of the heterojunction, but also for its photo stability. In fact, the improved interfacial electron transfer delocalizes the photogenerated holes also into the valence band of $Ag@TiO_2$, thus reducing the reported photocorrosion of Ag_3PO_4.

4. Conclusions

Heterojunction between silver doped TiO_2 ($Ag@TiO_2$) and Ag_3PO_4 has been proved to be a suitable candidate for photocatalytic remediation under solar light irradiation due to its outstanding photocatalytic activity. Physico-chemical characterization of the composites suggests the reasons of the superior performances with respect to the bare components and to the commercial benchmark TiO_2 P25 (Evonik). The optoelectronic features of the $Ag@TiO_2$–Ag_3PO_4 sample played a key role and determine its superior performances. In fact, fast charge transfer between the components resulted in efficient charge separation and higher photocatalytic efficiency. In particular, the photocatalytic activity of $Ag@TiO_2$–Ag_3PO_4 was higher than that of TiO_2–Ag_3PO_4. In fact, silver doping enables visible absorption also of the TiO_2 counterpart and resulted in the generation of higher amount of excitons localized on both $Ag@TiO_2$ and Ag_3PO_4 under solar light irradiation. This also improved spatial charge separation with respect to the TiO_2–Ag_3PO_4 sample, because electrons photogenerated in the conduction band of $Ag@TiO_2$ could now migrate toward the conduction band of Ag_3PO_4. For the outstanding photocatalytic activity highlighted in this work, $Ag@TiO_2$–Ag_3PO_4 could be proposed for solar light photocatalytic applications.

Supplementary Materials: The following are available online at http://www.mdpi.com/2079-4991/10/4/795/s1, Figure S1: XRD patterns of the TiO_2 sample. Figure S2: XRD patterns of the $Ag@TiO_2$ sample. Figure S3: XRD patterns of the Ag_3PO_4 sample. Figure S4: XRD patterns of the TiO_2–Ag_3PO_4 sample. Figure S5: EDS analysis of (a) Ag_3PO_4, (b,) $Ag@TiO_2$ and (c) $Ag@TiO_2$–Ag_3PO_4 samples.

Author Contributions: Conceptualization, A.H. and F.P.; methodology, A.R.; data analysis, R.C.; investigation, H.A.; data curation, R.C.; writing—original draft preparation, A.H.; writing—review and editing, F.P.; supervision, L.P.; funding acquisition, A.H. All authors have read and agreed to the published version of the manuscript.

Funding: This research was funded by: Encouragement of Young Researchers Project (PEJC) awarded to Dr. A. Hamrouni from the Tunisian Ministry of the Higher Education and Scientific Research.

Acknowledgments: L. Moschini and A. Elaziouti are kindly acknowledged for the SEM and EDS analyses.

Conflicts of Interest: The authors declare no conflict of interest. The funders had no role in the design of the study; in the collection, analyses, or interpretation of data; in the writing of the manuscript, or in the decision to publish the results.

References

1. Ahmad, T.; Farooq, U.; Phul, R. Fabrication and photocatalytic applications of perovskite materials with special emphasis on alkali-metal-based niobates and tantalates. *Ind. Eng. Chem. Res.* **2017**, *57*, 18–41. [CrossRef]
2. Guarisco, C.; Palmisano, G.; Calogero, G.; Ciriminna, R.; Di Marco, G.; Loddo, V.; Pagliaro, M.; Parrino, F. Visible-light driven oxidation of gaseous aliphatic alcohols to the corresponding carbonyls via TiO_2 sensitized by a perylene derivative. *Environ. Sci. Pollut. Res.* **2014**, *21*, 11135–11141. [CrossRef] [PubMed]
3. Abd-Elaal, A.; Parrino, F.; Ciriminna, R.; Loddo, V.; Palmisano, L.; Pagliaro, M. Alcohol-selective oxidation in water under mild conditions via a novel approach to hybrid composite photocatalysts. *ChemistryOpen* **2015**, *4*, 779–785. [CrossRef] [PubMed]

4. Yu, Y.; He, T.; Guo, L.; Yang, Y.; Guo, L.; Tang, Y.; Cao, Y. Efficient visible-light photocatalytic degradation system assisted by conventional Pd catalysis. *Sci. Rep.* **2015**, *5*, 9561. [CrossRef]
5. Bellardita, M.; El Nazer, H.; Loddo, V.; Parrino, F.; Venezia, A.; Palmisano, L.; El Nazer, H.A. Photoactivity under visible light of metal loaded TiO_2 catalysts prepared by low frequency ultrasound treatment. *Catal. Today* **2017**, *284*, 92–99. [CrossRef]
6. Liu, J.; de la Garza, L.; Zhang, L.; Dimitrijevic, N.M.; Zuo, X.; Tiede, D.M.; Rajh, T. Photocatalytic probing of DNA sequence by using TiO_2/dopamine-DNA triads. *Chem. Phys.* **2007**, *339*, 154–163. [CrossRef]
7. Carini, G.; Parrino, F.; Palmisano, G.; Scandura, G.; Citro, I.; Calogero, G.; Bartolotta, A.; Di Marco, G. Nanostructured anatase TiO_2 densified at high pressure as advanced visible light photocatalysts. *Photochem. Photobiol. Sci.* **2015**, *14*, 1685–1693. [CrossRef]
8. Guo, S.Q.; Hu, Z.; Zhen, M.; Gu, B.; Shen, B.; Dong, F. Insights for optimum cation defects in photocatalysis: A case study of hematite nanostructures. *Appl. Catal. B: Environ.* **2020**, *264*, 118506. [CrossRef]
9. Parrino, F.; Loddo, V.; Augugliaro, V.; Camera-Roda, G.; Palmisano, G.; Palmisano, L.; Yurdakal, S. Heterogeneous photocatalysis: Guidelines on experimental setup, catalyst characterization, interpretation, and assessment of reactivity. *Catal. Rev.* **2018**, *61*, 163–213. [CrossRef]
10. Parrino, F.; García-López, E.; Marcì, G.; Palmisano, L.; Felice, V.; Sora, I.N.; Armelao, L. Cu-substituted lanthanum ferrite perovskites: Preparation, characterization and photocatalytic activity in gas-solid regime under simulated solar light irradiation. *J. Alloy. Compd.* **2016**, *682*, 686–694. [CrossRef]
11. Ye, X.; Chen, Y.; Ling, C.; Zhang, J.; Meng, S.; Fu, X.; Wang, X.; Chen, S. Chalcogenide photocatalysts for selective oxidation of aromatic alcohols to aldehydes using O_2 and visible light: A case study of $CdIn_2S_4$, CdS and In_2S_3. *Chem. Eng. J.* **2018**, *348*, 966–977. [CrossRef]
12. Hamrouni, A.; Moussa, N.; Di Paola, A.; Parrino, F.; Houas, A.; Palmisano, L. Characterization and photoactivity of coupled ZnO–$ZnWO_4$ catalysts prepared by a sol–gel method. *Appl. Catal. B: Environ.* **2014**, *154*, 379–385. [CrossRef]
13. Hamrouni, A.; Moussa, N.; Di Paola, A.; Palmisano, L.; Houas, A.; Parrino, F. Photocatalytic activity of binary and ternary SnO_2–ZnO–$ZnWO_4$ composites. *J. Photochem. Photobiol. A: Chem.* **2015**, *309*, 47–54. [CrossRef]
14. Hamrouni, A.; Moussa, N.; Parrino, F.; Di Paola, A.; Houas, A.; Palmisano, L. Sol–gel synthesis and photocatalytic activity of ZnO–SnO_2 composites. *J. Mol. Catal. A: Chem.* **2014**, *390*, 133–141. [CrossRef]
15. Hamrouni, A.; Lachheb, H.; Houas, A. Synthesis, characterization and photocatalytic activity of ZnO–SnO_2 composites. *Mater. Sci. Eng. B.* **2013**, *178*, 1371–1379. [CrossRef]
16. Lachheb, H.; Ajala, F.; Hamrouni, A.; Houas, A.; Parrino, F.; Palmisano, L. Electron transfer in ZnO–Fe_2O_3 aqueous slurry systems and its effects on visible light photocatalytic activity. *Catal. Sci. Technol.* **2017**, *7*, 4041–4047. [CrossRef]
17. Parrino, F.; Bellardita, M.; García-López, E.I.; Marci, G.; Loddo, V.; Palmisano, L. Heterogeneous photocatalysis for selective formation of high-value-added molecules: Some chemical and engineering aspects. *ACS Catal.* **2018**, *8*, 11191–11225. [CrossRef]
18. Gou, J.; Ma, Q.; Cui, Y.; Deng, X.; Zhang, H.; Cheng, X.; Li, X.; Xie, M.; Cheng, Q.; Liu, H. Visible light photocatalytic removal performance and mechanism of diclofenac degradation by Ag_3PO_4 sub-microcrystals through response surface methodology. *J. Ind. Eng. Chem.* **2017**, *49*, 112–121. [CrossRef]
19. Seo, Y.; Yeo, B.-E.; Cho, Y.-S.; Park, H.; Kwon, C.; Huh, Y.-D. Photo-enhanced antibacterial activity of Ag_3PO_4. *Mater. Lett.* **2017**, *197*, 146–149. [CrossRef]
20. Bad'urová, K.; Monfort, O.; Satrapinskyy, L.; Dworniczek, E.; Gościniak, G.; Plesch, G. Photocatalytic activity of Ag_3PO_4 and some of its composites under non-filtered and UV-filtered solar-like radiation. *Ceram. Int.* **2017**, *43*, 3706–3712. [CrossRef]
21. Miyasato, R.; Fujiwara, M.; Sato, H.; Yano, T.; Hashimoto, H. Particle size effects of tetrahedron-shaped Ag_3PO_4 photocatalyst on water-oxidation activity and carrier recombination dynamics. *Chem. Phys. Lett. X* **2019**, *2*, 100023. [CrossRef]
22. Zwara, J.; Grabowska, E.; Klimczuk, T.; Lisowski, W.; Zaleska-Medynska, A. Shape-dependent enhanced photocatalytic effect under visible light of Ag_3PO_4 particles. *J. Photochem. Photobiol. A: Chem.* **2018**, *367*, 240–252. [CrossRef]
23. Luo, L.; Li, Y.; Hou, J.; Yang, Y. Visible photocatalysis and photostability of Ag_3PO_4 photocatalyst. *Appl. Surf. Sci.* **2014**, *319*, 332–338. [CrossRef]

24. Kubacka, A.; Fernández-García, M.; Colón, G. Advanced nanoarchitectures for solar photocatalytic applications. *Chem. Rev.* **2011**, *112*, 1555–1614. [CrossRef] [PubMed]
25. Palmisano, F.P.A.L. Reactions in the presence of irradiated semiconductors: Are they simply photocatalytic? *Mini-Rev. Org. Chem.* **2018**, *15*, 157–164.
26. Yao, W.; Zhang, B.; Huang, C.; Ma, C.; Song, X.; Xu, Q. Synthesis and characterization of high efficiency and stable Ag_3PO_4/TiO_2 visible light photocatalyst for the degradation of methylene blue and rhodamine B solutions. *J. Mater. Chem.* **2012**, *22*, 405–4055. [CrossRef]
27. Parrino, F.; De Pasquale, C.; Palmisano, L. Influence of surface-related phenomena on mechanism, selectivity, and conversion of TiO_2-induced photocatalytic reactions. *ChemSusChem* **2018**, *12*, 589–602. [CrossRef]
28. Rawal, S.B.; Do Sung, S.; Lee, W.I. Novel Ag_3PO_4/TiO_2 composites for efficient decomposition of gaseous 2–propanol under visible-light irradiation. *Catal. Commun.* **2012**, *17*, 131–135. [CrossRef]
29. Teng, W.; Li, X.; Zhao, Q.; Chen, G. Fabrication of $Ag/Ag_3PO_4/TiO_2$ heterostructure photoelectrodes for efficient decomposition of 2–chlorophenol under visible light irradiation. *J. Mater. Chem A.* **2013**, *1*, 9060–9068. [CrossRef]
30. Teng, W.; Li, X.; Zhao, Q.; Zhao, J.; Zhang, D. In situ capture of active species and oxidation mechanism of RhB and MB dyes over sunlight-driven Ag/ Ag_3PO_4 plasmonic nanocatalyst. *Appl. Catal. B: Environ.* **2012**, *125*, 538–545. [CrossRef]
31. Wu, M.-C.; Chan, S.-H.; Jao, M.-H.; Su, W.-F. Enhanced short-circuit current density of perovskite solar cells using Zn-doped TiO_2 as electron transport layer. *Sol. Energy Mater. Sol. Cells* **2016**, *157*, 447–453. [CrossRef]
32. Rtimi, S.; Baghriche, O.; Sanjines, R.; Pulgarin, C.; Bensimon, M.; Kiwi, J. TiON and TiON–Ag sputtered surfaces leading to bacterial inactivation under indoor actinic light. *J. Photochem. Photobiol. A: Chem.* **2013**, *256*, 52–63. [CrossRef]
33. Singh, S.; Singh, P.K.; Mahalingam, H. Novel floating Ag+ doped TiO2/polystyrene photocatalysts for the treatment of dye wastewater. *Ind. Eng. Chem. Res.* **2014**, *53*, 16332–16340. [CrossRef]
34. Goei, R.; Lim, T.-T. Ag-decorated TiO_2 photocatalytic membrane with hierarchical architecture: Photocatalytic and anti-bacterial activities. *Water Res.* **2014**, *59*, 207–218. [CrossRef]
35. Lei, X.; Xue, X.; Yang, H. Preparation and characterization of Ag-doped TiO_2 nanomaterials and their photocatalytic reduction of Cr(VI) under visible light. *Appl. Surf. Sci.* **2014**, *321*, 396–403. [CrossRef]
36. Mogal, S.I.; Gandhi, V.G.; Mishra, M.K.; Tripathi, S.; Shripathi, T.; Joshi, P.A.; Shah, D.O. Single-step synthesis of silver-doped titanium dioxide: Influence of silver on structural, textural, and photocatalytic properties. *Ind. Eng. Chem. Res.* **2014**, *53*, 5749–5758. [CrossRef]
37. Chang, L.-H.; Cho, C.-P. Enhanced photocatalytic characteristics by Ag-sensitized TiO_2 photocatalysts with mixed phases. *Mater. Chem. Phys.* **2019**, *223*, 683–693. [CrossRef]
38. Lutterotti, L.; Ceccato, R.; Maschio, R.D.; Pagani, E. Quantitative analysis of silicate glass in ceramic materials by the rietveld method. *Mater. Sci. Forum* **1998**, *278*, 87–92. [CrossRef]
39. Lutterotti, L. Total pattern fitting for the combined size–strain–stress–texture determination in thin film diffraction. *Nucl. Instrum. Methods Phys. Res. B: Beam Interact. Mater. At.* **2010**, *268*, 334–340. [CrossRef]
40. Tobaldi, D.M.; Pullar, R.C.; Gualtieri, A.F.; Seabra, M.P.; Labrincha, J.A. Phase composition, crystal structure, and microstructure of silver and tungsten doped TiO2 nanopowders with tunable photochromic behaviour. *Acta Mater.* **2013**, *61*, 5571–5585. [CrossRef]
41. Depero, L.E.; Sangaletti, L.; Allieri, B.; Blasenbauer, D.; Marino, A.; Zocchi, M. Correlation between crystallite sizes and microstrains in TiO_2 nanopowders. *J. Cryst. Growth* **1999**, *198*, 516–520. [CrossRef]
42. Ahmad, A.; Thiel, J.; Shah, S.I. Structural effects of niobium and silver doping on titanium dioxide nanoparticles. *J. Physics: Conf. Ser.* **2007**, *61*, 11–15. [CrossRef]
43. Ajala, F.; Hamrouni, A.; Houas, A.; Lachheb, H.; Megna, B.; Palmisano, L.; Parrino, F. The influence of Al doping on the photocatalytic activity of nanostructured ZnO: The role of adsorbed water. *Appl. Surf. Sci.* **2018**, *445*, 376–382. [CrossRef]
44. Dhanabal, R.; Chithambararaj, A.; Velmathi, S.; Bose, A.C. Visible light driven degradation of methylene blue dye using Ag_3PO_4. *J. Environ. Chem. Eng.* **2015**, *3*, 1872–1881. [CrossRef]
45. Liang, Q.; Ma, W.; Shi, Y.; Li, Z.; Yang, X. Hierarchical Ag_3PO_4 porous microcubes with enhanced photocatalytic properties synthesized with the assistance of trisodium citrate. *CrystEngComm* **2012**, *14*, 2966. [CrossRef]

46. Tom, R.T.; Nair, A.S.; Singh, N.; Aslam, M.; Nagendra, C.L.; Philip, R.; Vijayamohanan, K.; Pradeep, T. Freely dispersible Au@TiO2, Au@ZrO2, Ag@TiO2, and Ag@ZrO2, core-shell nanoparticles: One-step synthesis, characterization, spectroscopy, and optical limiting properties. *Langmuir* **2003**, *19*, 3439–3445. [CrossRef]
47. Jia, L.; Wu, C.; Li, Y.; Han, S.; Li, Z.; Chi, B.; Pu, J.; Jian, L. Enhanced visible-light photocatalytic activity of anatase TiO_2 through N and S coupling. *Appl. Phys. Lett.* **2011**, *98*, 211903. [CrossRef]
48. Yi, Z.; Ye, J.; Kikugawa, N.; Kako, T.; Ouyang, S.; Stuart-Williams, H.; Yang, H.; Cao, J.; Luo, W.; Li, Z.; et al. An orthophosphate semiconductor with photooxidation properties under visible-light irradiation. *Nat. Mater.* **2010**, *9*, 559–564. [CrossRef]
49. Liu, J.; Fu, X.; Chen, S.F.; Zhu, Y.F. Electronic structure and optical properties of Ag_3PO_4 photocatalyst calculated by hybrid density functional method. *Appl. Phys. Lett.* **2011**, *99*, 191903. [CrossRef]
50. Dorothy, A.A.; Subramaniam, N.G.; Panigrahi, P.; Subramaniam, G. Tuning electronic and optical properties of TiO_2 with Pt/Ag doping to a prospective photocatalyst: A first principles DFT study. *Mater. Res. Express* **2019**, *6*, 045913. [CrossRef]
51. Ji, P.; Takeuchi, M.; Cuong, T.-M.; Zhang, J.; Matsuoka, M.; Anpo, M. Recent advances in visible light-responsive titanium oxide-based photocatalysts. *Res. Chem. Intermed.* **2010**, *36*, 327–347. [CrossRef]
52. Tada, H.; Jin, Q.; Nishijima, H.; Yamamoto, H.; Fujishima, M.; Okuoka, S.-I.; Hattori, T.; Sumida, Y.; Kobayashi, H. Titanium(IV) dioxide surface-modified with iron oxide as a visible light photocatalyst. *Angew. Chem. Int. Ed.* **2011**, *50*, 3501–3505. [CrossRef] [PubMed]
53. Roy, A. Determination of the flatband potential of semiconductor particles in suspension by photovoltage measurement. *Int. J. Hydrogen Energy* **1995**, *20*, 627–630. [CrossRef]
54. Li, Y.; Wang, P.; Huang, C.; Yao, W.; Wu, Q.; Xu, Q.-J. Synthesis and photocatalytic activity of ultrafine Ag_3PO_4 nanoparticles on oxygen vacated TiO_2. *Appl. Catal. B: Environ.* **2017**, *205*, 489–497. [CrossRef]
55. Chen, X.; Dai, Y.; Wang, X. Methods and mechanism for improvement of photocatalytic activity and stability of Ag_3PO_4: A review. *J. Alloy. Compd.* **2015**, *649*, 910–932. [CrossRef]
56. Kisch, H.; Burgeth, G.; Macyk, W. Visible light photocatalysis by a titania transition metal complex. *Adv. Inorg. Chem.* **2004**, *56*, 241–259.